HiSST: 3rd International Conference on
High-Speed Vehicle Science Technology
14 -19 April 2024, Busan, Korea

An Investigation of Internal Drag Correction Methodology for Wind Tunnel Test Data in a High-Speed Air-Breathing Vehicle using Numerical Analysis

Younghwan Lee[1], Hyeon Jin[2], Min-Gyu Kim[3], Hyungrok Do[4]

Abstract

Accurate understanding of aerodynamic characteristics is critical for air vehicle design. This study applies the impulse-momentum theorem to estimate internal drag of an asymmetric air vehicle. Both computational fluid dynamics (CFD) and wind tunnel tests were employed. Numerical analysis using STAR-CCM+ was conducted across various Mach numbers, while wind tunnel tests were conducted under only specific Mach number conditions. The measured data from wind tunnel tests, which is considered representative, were compared with CFD plane-averaged values, indicating fairly good agreement. However, discrepancies arose when comparing CFD cell-averaged values with the plane-averaged values. To address this, a correction function was developed to describe the differences. It was observed that the ratio of internal drag coefficient from the cell-averaged values to that of the plane-averaged values followed an exponential function of Mach number. This approach allows wind tunnel data to be transformed into a form akin to cell-averaged values, enhancing internal drag estimation accuracy. Future research will explore additional methodologies to further refine and validate the proposed approach.

Keywords: *Internal drag correction, Flow-through model analysis, CFD analysis, Wind tunnel test*

Nomenclature

A – Area
C_x – Drag coefficient at x-direction
M – Mach number
MFR – Mass flow rate ratio
$\dot{m}$ – Mass flow rate
P – Static pressure
P_t – Total pressure
q – Dynamic pressure
T – Thrust
v – Velocity

Subscripts
0 – Far-field
1 – Inlet
2 – Exit
c – Cowl
c-avg – Cell-averaged
i – Internal
p-avg – Plane-averaged
ref – Reference
x – x-direction

Greek
α – Angle of attack
θ – Exit flow angle

1. Introduction

In the air vehicle design process, a thorough comprehension of the aerodynamic characteristics acting on the vehicle is essential. These characteristics not only influence the vehicle configurations but also

[1] Agency for Defence Development and Seoul National University, *34186 Yuseong P.O.box Daejeon, Rep. of Korea, yhlee0706@snu.ac.kr*
[2] Agency for Defence Development, *34186 Yuseong P.O.box Daejeon, Rep. of Korea, jheon0821@gmail.com*
[3] Agency for Defence Development, *34186 Yuseong P.O.box Daejeon, Rep. of Korea, f22ace@gmail.com*
[4] Seoul National University, *Building 301, 1, Gwanak-ro, Gwanak-gu, Seoul, Rep. of Korea, hyungrok@snu.ac.kr*

significantly impact maneuverability and trajectory [1]. For air vehicles with air-breathing engines, obtaining precise external drag data is crucial for making informed design decisions. However, measuring external drag directly is nearly impossible; therefore, engineers typically measure the total drag and subtract the internal drag component.

To this end, the impulse-momentum theorem, which relates forces to changes in momentum, has been widely adopted as bookkeeping method among aerodynamic engineers and engine designers to calculate internal drag [2-4]. Zhang et al. applied the thrust-drag bookkeeping method in computational fluid dynamics to decompose thrust and drag in their aircraft model, revealing lift and drag variations under different power conditions [2]. Similarly, Malouin et al utilized the thrust-drag bookkeeping method to decompose internal, external, and waked drag, introducing a new control volume that did not strictly consider the stagnation line [3]. Goulos et al. employed the thrust-drag bookkeeping approach to comprehend the aerodynamic characteristics of combined engine-airframe architectures, categorizing the effects on the frame, nacelle, and exhaust [4]. However, these studies primarily focused on decomposing elements. In contrast to the computational studies, Jin utilized three probes in experimental wind tunnel tests to measure exit properties and calculate internal drag for an asymmetric vehicle [5]. Similarly, Lee investigated designing a flow-through model for measuring internal properties experimentally [6]. However, these experimental studies solely focused on measurements and model designs. Previous work has not thoroughly examined the potential disparities between experimental and computational outcomes. Identifying correlations among these results is an area that merits further investigation.

In wind tunnel tests, obtaining representative properties at the exit of the nozzle poses significant challenges. This difficulty arises not only due to size limitations of the model within the test facilities but also because of the complexity of the flow, including phenomena such as flow separation and unsteadiness. Papamoschou et al. and Xiao et al. conducted numerical investigations of flow separation in a symmetric nozzle and compared their results with experimental results [7, 8]. They identified flow separation and shock locations numerically, which were subsequently validated through experimental data. However, their studies focused solely on comparing static pressure at the nozzle wall and shadow graphs.

Notably, numerical analysis offers both plane-averaged values, aligning with wind tunnel measurements, and cell-averaged values exclusive to numerical analysis. Applying these different averaging approaches within the impulse-momentum theorem may introduce gaps in accurately reconciling computational and experimental results, which is crucial for calculating external drag. Therefore, this study aims to bridge this gap by comprehensively analyzing the disparities between plane-averaged and cell-averaged values, and presenting them in a numerical fitting form to develop a correction methodology.

In this investigation, the impulse-momentum theorem known as bookkeeping method was applied to an asymmetric vehicle, and internal drag was calculated through wind tunnel test and numerical analysis in order to obtain accurate external aerodynamic characteristics. During the wind tunnel test, properties at the asymmetric exit were measured at the mid-point, due to the limited size of model and disturbance induced by sensors. In the numerical analysis, plane-averaged values and cell-averaged values were used to calculate internal drag. The results from the wind tunnel test showed reasonable agreement with the plane-averaged values in terms of internal drag calculations. However, some disparities arose between the plane-averaged and cell-averaged values, likely due to flow distortion at the asymmetric exit. Therefore, this study primarily focuses on analyzing the differences between cell-averaged and plane-averaged values from numerical analysis. The goal is to establish a correction relation as a function of Mach number, thereby enhancing the precision of external drag calculations obtained from wind tunnel data.

2. Internal Drag Correction

2.1. Internal Drag

Internal drag is a crucial factor in air vehicles equipped with air-breathing engines, representing the drag experienced within the vehicle's flow-through channel. According to the net thrust equation (Eq. 1), the incoming momentum from the far-field is inherently considered. Thereby, the internal drag is

already incorporated within the thrust component. Thus, including internal drag in aerodynamic data would result in double counting.

$$T = (\dot{m}_2 v_2 - \dot{m}_0 v_0) + A_2(p_2 - p_0) \quad (1)$$

However, ignoring the presence of internal channels poses a significant challenge, particularly during wind tunnel tests imitating actual external flow around an intake. Wind tunnel models with modified intakes, such as closed intakes, may not be able to capture the actual flow field around the inlet, resulting in difference in pressure gradients on the model. Consequently, wind tunnel tests are conducted with models typically include internal channels. Subsequently, internal terms are excluded during post-processing to avoid double counting. Further details on this methodology can be found in reference [6]. Figure 1 visually illustrates the distinction between internal and external locations within the test model.

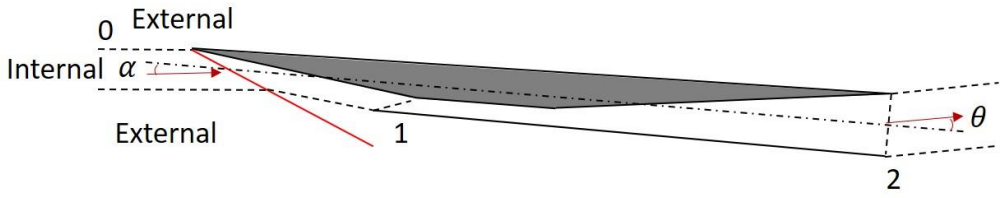

Fig 1. Internal and external location

To evaluate internal drag, the impulse-momentum theorem is employed (Eq. 2). By assessing the impulse and the momentum difference between the exit and the far-field, along with the gauge pressure at the exit, the internal drag can be calculated. In this study, both wind tunnel tests and CFD analysis were conducted to measure and calculate the required properties, respectively.

$$C_{xi} = \frac{(\dot{m}_0 v_{x_0} - \dot{m}_2 v_{x_2}) + A_2(p_0 - p_2)}{q A_{ref}} \quad (2)$$

2.2. Wind Tunnel Test

In this study, the wind tunnel tests were conducted in a high speed wind tunnel. The high speed wind tunnel is a blow-down type wind tunnel and as shown in Figure 2, it consists of an air storage tank, a heater, a nozzle, a test section, a diffuser, a cooler and a vacuum tank. The Mach number can be changed by replacing the nozzle and the Reynolds number for the test conditions can be obtained by controlling the pressure and the temperature of the settling chamber. The high speed wind tunnel uses high temperature gas at the level to prevent air condensation and it cannot be heated to the level of high enthalpy of the flight test conditions due to the limitations in the heater. In general, high speed wind tunnels require high pressure air in front of the settling chamber and low pressure air, almost a vacuum behind the settling chamber. The settling chamber pressure is determined by the Reynolds number and before the test, the pressure of the test section must be a sufficient vacuum condition to form the desired flow in the test section through the nozzle. The compressed air in front of the settling chamber is heated to a high temperature test air by the heater, and the pressure and temperature are controlled by releasing the compressed air to the outside until the test conditions are reached. When the set pressure and temperature are reached, the valve in the path through which the gas is released to the outside is closed, and the valve in the direction toward the nozzle and the test section is opened. The test air which is high temperature and high pressure flows into the test section [9].

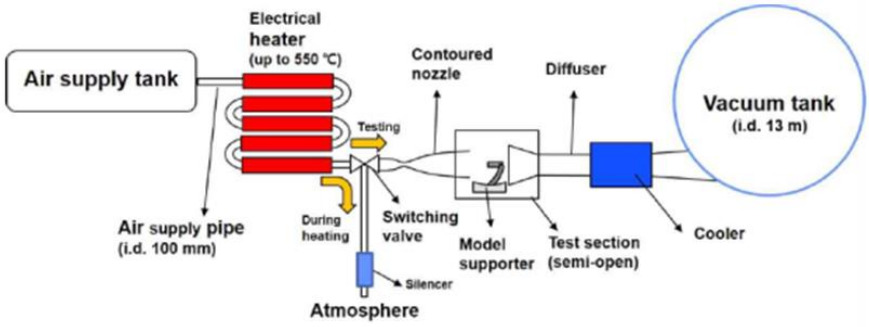

Fig 2. Layout of the high speed wind tunnel

To accurately determine internal drag, it is essential to understand the flow characteristics at the exit of the vehicle nozzle, as depicted in Fig. 1. In the wind tunnel test, we conducted measurements of total pressure and static pressure at the exit. While the internal flow of the vehicle ideally runs parallel to the external flow, the asymmetric nozzle geometry induces a flow angle at the exit, necessitating precise measurement techniques.

The wind tunnel test utilized three types of probes: one for wind direction measurement, another for total pressure, and the third for static pressure. Due to the model's size, the wind was blown four times under identical conditions for each probe. Initially, the wind direction was measured using a wedge probe with varying probe angles. As shown in Fig. 3(a), the pressure difference between the upper and lower surfaces of the wedge probe determines the flow angle at the exit when it becomes zero. Subsequently, static pressure and total pressure were measured using a cone probe and pitot probe, respectively. It's important to note that the pressure measured by the sharp cone probe is not static pressure. Instead, static pressure was derived using the Taylor-Maccoll equation based on the apex angle of the cone, cone pressure, and total pressure measured by the pitot probe. The probes are described in the Fig. 3.

Four sensors (two in the wedge probe, one each in the cone probe and pitot probe) were employed in the test. To ensure precise pressure measurement, sensors with lower full-scale pressure were selected for probes expected to measure low pressure. Probes were positioned as close to the center of the nozzle exit as possible, with the hole in the x-axis direction aligned with the nozzle exit surfaces.

Using total pressure, static pressure, and flow angle measurements, internal drag coefficient can be calculated using Eq. (3) derived from Eq. (2). Additionally, the mass flow rate ratio (MFR) can be calculated using Eq. (4). Further details regarding the test methodology can be found in reference [5].

$$C_{xi} = A_c \frac{\left(\gamma p_0 {M_0}^2 MFR \cos\alpha - \gamma p_2 {M_2}^2 \frac{A_2}{A_c}\cos\theta\right) + \frac{A_2}{A_c}(p_0 - p_2)}{q A_{ref}} \tag{3}$$

$$MFR = \frac{\dot{m}_i}{\dot{m}_c} = \frac{A_0}{A_c} \tag{4}$$

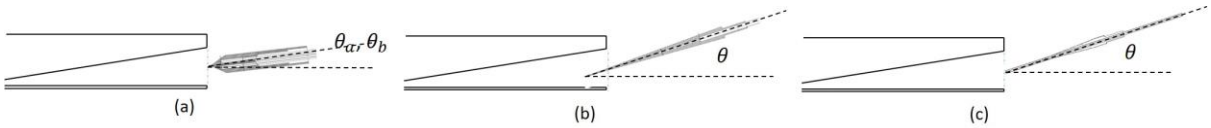

Fig 3. Three probes: (a) wedge probe, (b) cone probe, (c) pitot probe

2.3. Numerical Analysis

In this study, steady-state computations were performed for various Mach numbers using the commercial software STAR-CCM+. Temperature and pressure were assumed to adhere to standard

atmospheric conditions. The computational configuration mirrored that of the wind tunnel test model. To maintain a balance between numerical cost and accuracy, a grid dependency test was conducted. Figure 4 illustrates the variations in mass flow rate ratio resulting from different grid sizes. In this study, a grid consisting of 1.3 million polynomial cells with 17 prism layers was selected. The analysis addressed the Reynolds-averaged compressible Navier-Stokes equations with the K-ω SST turbulence model and ASUM+ Scheme, as the K-ω SST turbulence model offers improved flow separation prediction [10]. The computational grid and Mach number fields are depicted in Figures 5 and 6.

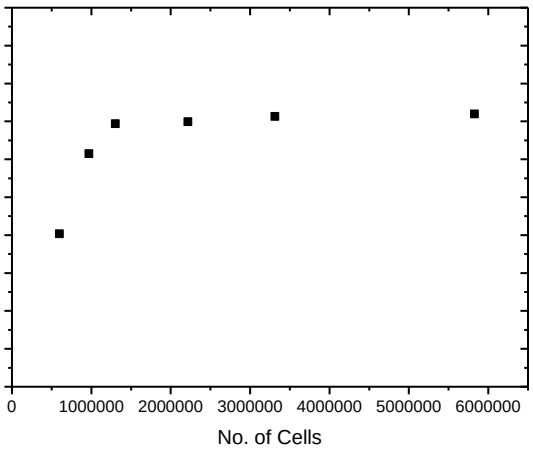

Fig 4. Grid test

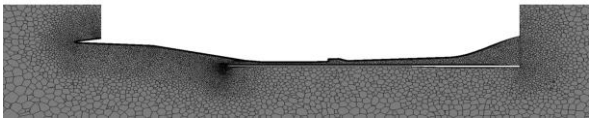

Fig 5. Computational grid

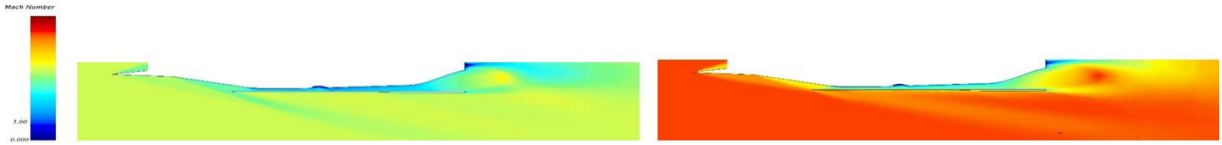

Fig 6. Mach contour for Case 2(left) and Case 4(right)

Since the measured properties in the wind tunnel test serve as representative values of the measured plane, it is essential to calculate the internal drag using both plane-averaged and cell-averaged values at the exit and compare them. The plane-averaged values correspond to the measured data from the wind tunnel test, while the cell-averaged values can only be obtained through CFD. To incorporate these values into "Eq.2", the momentum equation can be articulated in "Eq. 5" and "Eq. 6". From the definition of impulse-momentum theorem, it is more appropriate to utilize the drag coefficient obtained from the cell-averaged values. Consequently, by considering the difference between each averaging method, internal drag calculated from wind tunnel data can be transformed into that of the cell-averaged values.

$$C_{xi,p-avg} = \frac{(\bar{\dot{m}}_0 \bar{v}_{x_0} - \bar{\dot{m}}_2 \bar{v}_{x_2}) + A_2(\bar{p}_0 - \bar{p}_2)}{qA_{ref}} \tag{5}$$

$$C_{xi,c-avg} = \frac{(\sum \dot{m}_0 v_{x_0} - \sum \dot{m}_2 v_{x_2}) + \sum A_2(p_0 - p_2)}{qA_{ref}} \tag{6}$$

3. Results

In this study, wind tunnel tests and CFD analysis were conducted across various Mach numbers, all within the supersonic region. In Table 1, a summary of internal drag coefficients obtained at zero angle of attack from both wind tunnel testing and numerical analysis are presented. For numerical analysis, four Mach numbers were selected: Cases 1 through 4, with each subsequent case representing an increase in Mach number. Specifically, flow conditions for Cases 3 and 4 were chosen in the wind tunnel tests.

Table 1. Internal drag coefficient for each case

	Case 1	**Case 2**	**Case 3**	**Case 4**
Wind Tunnel			0.0241	0.0277
CFD p-avg.	0.0135	0.0236	0.0238	0.0270
CFD c-avg.	0.0131	0.0226	0.0208	0.0221

In case 3 and 4, internal drag coefficients calculated from the plane-averaged values in the numerical analysis were slightly lower than those obtained from the wind tunnel tests across all angles of attack. Nevertheless, the comparison between the two sets of data showed reasonable agreement, as depicted in Fig. 7. These findings indicate that the numerical results of the plane-averaged values closely approximate those derived from the wind tunnel tests.

Although wind tunnel test and the plane-averaged internal drag coefficients exhibited similar trends, a noticeable difference was observed in the case of the cell-averaged internal drag (Fig. 8). Fig. 8 describes the difference observed at zero angle of attack across all Cases 1 through 4, becoming more significant with increasing Mach numbers. This suggests that the internal drag calculation using the plane-averaged values and that obtained from wind tunnel measurements may not fully account for the flow distortion at the exit.

To better understand this difference, flow patterns were analyzed. Fig. 9 illustrates the flow patterns at the exit, showing that the majority of the flow follows along the bottom of the channel (Fig. 9(a)). The mass flow rate at the calculated points is non-dimensionalized by the total mass flow rate, as depicted in Fig. 9(a). At higher Mach numbers, a greater proportion of the flow is concentrated along the bottom of the channel compared to lower Mach numbers. This phenomenon can be attributed to the higher momentum of the flow at higher Mach numbers, which propels the fluid to persistently advance along the axial direction, even in the presence of an asymmetric nozzle.

This observation is further supported by the total pressure ratio (TPR) profiles depicted in Fig. 9(c). In high Mach number cases, the total pressure ratio near the top wall is drastically decreased compared to that at low Mach numbers. Consequently, at low Mach numbers, the flow tends to adhere more closely to the nozzle geometry, resulting in reduced flow distortion. The total pressure ratio can be described as the ratio of the total pressure at the calculated points to the total pressure at the far-field (Eq. 7).

Velocity profiles also corroborate this observation (Fig. 9(b)). To compare velocities across different Mach numbers, each velocity component was non-dimensionalized by the freestream velocities. Despite the velocity profiles showing relative uniformity compared to other properties, a notable difference was observed between the velocities near the bottom and upper walls; the flow near the bottom wall was faster than that near the upper wall.

Similarly, static pressure was non-dimensionalized by the freestream pressure (Eq. 8), with the highest static pressure observed near the bottom of the channel. This pressure gradually decreases towards the upper surface before abruptly rising towards the upper wall (Fig. 9(d)). For high Mach numbers, the rise in static pressure near the upper wall was too rapid, potentially causing the flow to be unable to adhere to the upper wall.

$$TPR = \frac{P_t}{P_{t,inf}} \tag{7}$$

$$PR = \frac{P}{P_{inf}} \tag{8}$$

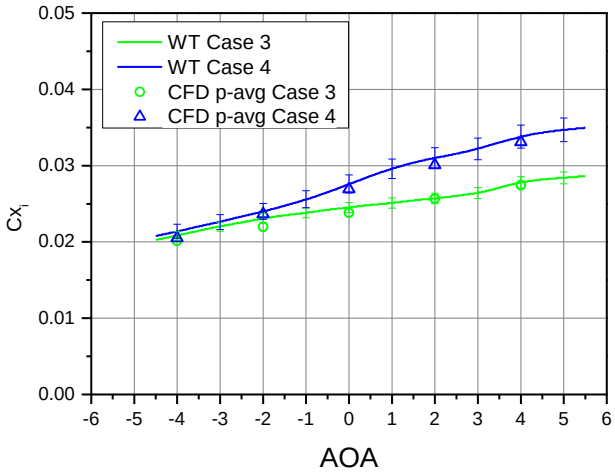

Fig 7. Internal drag coefficient comparison between wind tunnel test and the plane-averaged result.

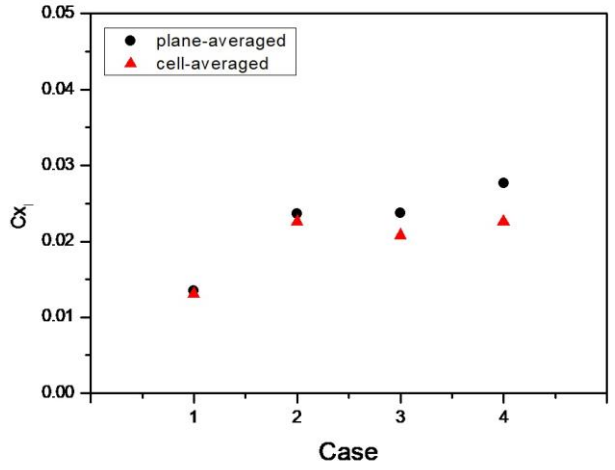

Fig 8. Plane-averaged internal drag coefficient and cell-averaged internal drag coefficient

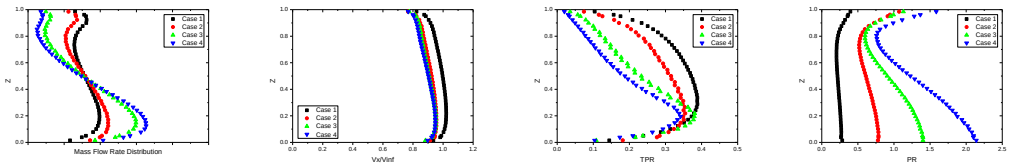

(a) (b) (c) (d)

Fig 9. (a)Mass flow rate distribution, (b)x-directional velocity distribution, (c)total pressure distortion and (d)static pressure distortion from the bottom to the top at the exit

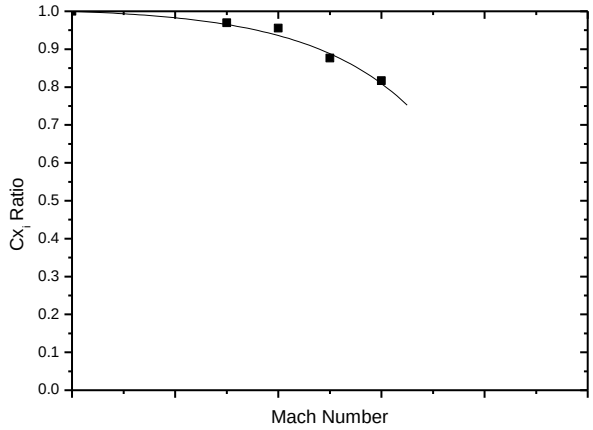

Fig 10. Difference and correction function

As a result, as Mach number increases, the flow distortion becomes more significant, leading to a greater disparity between the internal drag based on the plane-averaged values and that based on the cell-averaged values. The difference rate is defined as the ratio of internal drag from the cell-averaged value and that of the plane-averaged value (Eq. 9).

$$C_{xi,rate} = \frac{C_{xi,c-avg}}{C_{xi,p-avg}} \tag{9}$$

The discrepancy between the averaged values can be expressed as a function of Mach number when the angle of attack is zero, as shown in Fig. 10. Assuming no flow, there would be no differences, leading to an estimated disparity of zero. However, as Mach number increases, the difference exponentially grows. Consequently, the internal drag coefficient can be corrected using an exponential form derived from the fitting curve (Eq. 10).

$$f_{corr} = 1.01 - 0.01e^{0.5M} \tag{10}$$

4. Conclusions and Discussions

Previous studies have utilized the impulse-momentum theorem as a Bookkeeping method to decompose internal and external drag in their vehicles. However, these studies have typically focused on applying the method on either through CFD computation or wind tunnel tests. Some studies have compared wind tunnel test results with numerical analysis, but these comparisons have primarily focused on wall pressures and shadowgraphs.

In this study, internal drag coefficient was obtained through wind tunnel tests and numerical analysis using the impulse-momentum theorem. While the results from wind tunnel test appeared to align well with the plane-averaged values from CFD analysis, theoretical considerations suggest that the internal drag coefficient obtained from the cell-averaged values are more reasonable.

To address this, a correction fitting function was developed to quantify and analyze the observed relation between the internal drag coefficient calculated from the plane-averaged values and that from the cell-averaged values. This correction function allows the internal drag coefficient obtained from wind tunnel test data to account for flow distortion, resulting in more precise results that can be reconciled with the cell-averaged values from computational fluid dynamics analysis.

To sum, this study introduces a proper methodology for employing the impulse-momentum theorem in wind tunnel tests and provides a correction function to calculate more precise internal and external drag. The findings from this study have the potential to modify the approach to using wind tunnel test results in internal drag estimation.

Although the correction fitting function might have limitations specific to the geometry, flow conditions and measurement locations studied here, the overall method itself shows promise in enhancing the accuracy of the impulse-momentum theorem in wind tunnel tests. In future work, this method will be applied to various geometries including axisymmetric exit to extend the correction function and further improve the applicability of this approach.

Acknowledgements

This work was supported by the Korean Government.

References

1. Young, A.D., Paterson, J. H., Jones, J. L.: Aircraft excrescence drag, North Atlantic Treaty Organization (NATO), Advisory Group for Aerospace Research and Development (AGARD), Technical Report AGARD-AG-264, Bruxelles, Belgium (1981)
2. Zhang, Y., Chen, H., Li, Z., Zhang, M., Zhang, M., Fu, S.: A thrust drag bookkeeping method based on computational fluid dynamics, AIAA Propulsion and Energy Forum, July 28-30, Cleveland, OH, 50th AIAA/ASME/ASE/ASEE Joint Propulsion Conference (2014)
3. Malouin, B., Gariepy, M., Trepanier, J., Laurendeau, E.: Internal drag devaluation for a through-flow nacelle using a far-field approach, Journal of Aircraft Vol. 52, No. 6, 1847-1857 (2015)
4. Goulos, I., Otter, J., Tejero, F., Rebassa, J. H., MacManus, D., Sheaf, C.: Civil turbofan propulsion aerodynamics: thrust-drag accounting and impact of engine installation position, Aerospace Science and Technology 111, (2021) 106533
5. Jin, H.: An experimental study on internal drag correction of high speed vehicle using three probes, J. Korean Soc. Aeronaut. Space Sci. 49(7), 529-537(2021)
6. Lee, Y.: A numerical study on flow-through model design considering the internal loss, International Journal of Aeronautical and Space Science Vol. 20, No. 3, 688-696(2019)
7. Papamoschou, D., and Zill, A.: Fundamental Investigation of Supersonic Nozzle Flow Separation, AIAA Paper 2004-1111, Jan. 2004.
8. Xiao, Q., Tsai, H. M., and Papamoschou. D.: Numerical Investigation of Supersonic Nozzle Flow Separation, AIAA Journal Vol. 45, No. 3, 532-541(2007)
9. Kim, S. H., Kim, Y. J., Lee, J. G. and Kim, N. G.: Introduction of ADD Hypersonic Wind Tunnel, Proceeding of The Korean Society for Aeronautical and Space Sciences Spring Conference, November 2017, pp. 23~25
10. Arif, I., Iftikhar, H., and Javed, A.: Design and optimization of bump (compression surface) for divertless supersonic inlet, Proc. IMechE Part G, J. Aerospace Engineering, 236(I) 33-48(2022) doi.org/10.1177/09544100211002970